

Near-perfect absorption in epsilon-near-zero structures with hyperbolic dispersion

Klaus Halterman^{1,*} and J. Merle Elson²

¹*Michelson Lab, Physics Division, Naval Air Warfare Center, China Lake, California 93555, USA*

²*PO Box 965, Tijeras, New Mexico 87059, USA*

[*klaus.halterman@navy.mil](mailto:klaus.halterman@navy.mil)

Abstract: We investigate the interaction of polarized electromagnetic waves with hyperbolic metamaterial structures, whereby the in-plane permittivity component ϵ_x is opposite in sign to the normal component ϵ_z . We find that when the thickness of the metamaterial is smaller than the wavelength of the incident wave, hyperbolic metamaterials can absorb significantly higher amounts of electromagnetic energy compared to their conventional counterparts. We also demonstrate that for wavelengths leading to $\Re(\epsilon_z) \approx 0$, near-perfect absorption arises and persists over a range of frequencies and subwavelength structure thicknesses.

© 2021 Optical Society of America

OCIS codes: (160.3918) Metamaterials; (160.1190) Anisotropic optical materials.

References and links

1. D. Sievenpiper, L. Zhang, R. Broas, N. G. Alexopolous, and E. Yablonovitch, "High-impedance electromagnetic surfaces with a forbidden frequency band," *IEEE Trans. Microwave Theory Tech.* **47**(11), 20592074 (1999).
2. M. G. Silveirinha and N. Engheta, "Tunneling of electromagnetic energy through subwavelength channels and bends using ϵ -near-zero materials," *Phys. Rev. Lett.* **97**(15), 157403 (2006).
3. K. Halterman and S. Feng, "Resonant transmission of electromagnetic fields through subwavelength zero- ϵ slits," *Phys. Rev. A* **78**, 021805(R) (2008).
4. K. Halterman, S. Feng, and V. C. Nguyen, "Controlled leaky wave radiation from anisotropic epsilon near zero metamaterials," *Phys. Rev. B* **84**, 075162 (2011).
5. S. Feng and K. Halterman, "Coherent perfect absorption in epsilon-near-zero metamaterials," *Phys. Rev. B* **86**, 165103 (2012).
6. D. Schurig and D. R. Smith, "Spatial filtering using media with indefinite permittivity and permeability tensors," *Appl. Phys. Lett.* **82**, 2215-2217 (2003).
7. C. L. Cortes, W. Newman, S. Molesky, and Z. Jacob, "Quantum nanophotonics using hyperbolic metamaterials," *J. Opt.* **14**(6), 063001 (2012).
8. Y. Liu, G. Bartal, and X. Zhang, "All-angle negative refraction and imaging in a bulk medium made of metallic nanowires in the visible region," *Opt. Express* **16**(20), 1543915448 (2008).
9. I. Nefedov and S. Tretyakov, "Ultrabroadband electromagnetically indeterminate medium formed by aligned carbon nanotubes," *Phys. Rev. B* **84**(11), 113410 (2011).
10. X. Ni, S. Ishii, M. D. Thoreson, V. M. Shalaev, S. Han, S. Lee, and A. V. Kildishev, "Loss-compensated and active hyperbolic metamaterials," *Opt. Express* **19**(25), 2524225254 (2011).
11. S. Savoia, G. Castaldi, and V. Galdi, "Optical nonlocality in multilayered hyperbolic metamaterials based on Thue-Morse superlattices," *Phys. Rev. B* **87**, 235116 (2013).
12. O. Kidwai, S. V. Zhukovsky, and J. E. Sipe, "Effective-medium approach to planar multilayer hyperbolic metamaterials: Strengths and limitations," *Phys. Rev. A* **85**(5), 053842 (2012).
13. W. Yan, M. Wubs, and N. A. Mortensen, "Hyperbolic metamaterials: nonlocal response regularizes broadband supersingularity," *Phys. Rev. B* **86**, 205429 (2012).

14. T. Tumkur, L. Gu, J. Kitur, E. Narimanov, and M. Noginov, "Control of absorption with hyperbolic metamaterials," *Appl. Phys. Lett.* **100**, 161103161108 (2012).
 15. F. V. Iorsh, I. S. Mukhin, I. V. Shadrivov, P. A. Belov, and Y. S. Kivshar, "Hyperbolic metamaterials based on multilayer graphene structures," *Phys. Rev. B* **87**(7), 075416 (2013).
 16. W. Li, Z. Liu, X. Zhang, and X. Jiang, "Switchable hyperbolic metamaterials with magnetic control," *Appl. Phys. Lett.* **100**, 1611084 (2012).
 17. C. Rizza, A. Ciattoni, E. Spinozzi, and L. Columbo, "Terahertz active spatial filtering through optically tunable hyperbolic metamaterials," *Opt. Lett.* **37**, 33453347 (2012).
 18. C. Rizza, A. Ciattoni, L. Columbo, M. Brambilla, and F. Prati, "Terahertz optically tunable dielectric metamaterials without microfabrication," *Opt. Lett.* **38**, 1307 (2013).
 19. W. Yan, L. Shen, L. Ran, and J. A. Kong, "Surface modes at the interfaces between isotropic media and indefinite media," *J. Opt. Soc. Am. A* **24**, 530 (2007).
 20. K.V. Sreekanth, A. De Luca, and G. Strangi, "Experimental demonstration of surface and bulk plasmon polaritons in hypergratings," *Sci. Rep.* **3**, 3291 (2013).
 21. E. Narimanov, M. A. Noginov, H. Li, and Y. Barnakov, "Darker than Black: Radiation-absorbing Metamaterial," in *Quantum Electronics and Laser Science Conference, OSA Technical Digest (CD)* (Optical Society of America, 2010), paper QPDA6.
 22. T. U. Tumkur, J. K. Kitur, B. Chu, L. Gu, V. A. Podolskiy, E. E. Narimanov, and M. A. Noginov, "Control of reflectance and transmittance in scattering and curvilinear hyperbolic metamaterials," *Appl. Phys. Lett.* **101**, 091105 (2012).
 23. J. M. Zhao, Y. Chen, and Y. J. Feng, "Polarization beam splitting through an anisotropic metamaterial slab realized by a layered metal-dielectric structure," *Appl. Phys. Lett.* **92**, 071114 (2008).
 24. G. V. Naik, J. Liu, A. V. Kildishev, V. M. Shalaev, and A. Boltasseva, "Demonstration of Al:ZnO as a plasmonic component for near-infrared metamaterials," *Proc. Natl. Acad. Sci. U.S.A.* **109**(23), 88348838 (2012).
 25. J. P. Berenger, "A perfect matched layer for the absorption of electromagnetic waves," *J. Comput. Phys.* **114**, 185200 (1994).
 26. Z. Sacks, D. M. Kingsland, R. Lee, and J. F. Lee, "A perfectly matched anisotropic absorber for use as an absorbing boundary condition," *IEEE Trans. Ant. Prop.* **43**, 14601463, (1995).
 27. J. Merle Elson, "Propagation in planar waveguides and the effects of wall roughness," *Opt. Express* **9**, 461-475 (2001).
 28. J. M. Elson, *Proc. SPIE 4780, Surface Scattering and Diffraction for Advanced Metrology II*, **32**, (October 1, 2002).
 29. Y. Jin, S. Xiao, N.A. Mortensen, and S. He, "Arbitrarily thin metamaterial structure for perfect absorption and giant magnification," *Opt. Express* **19**, 11114 (2011).
 30. See, for example, J. D. Jackson, *Classical Electrodynamics*, Third Edition Wiley and Sons
 31. D. R. Smith and D. Schurig, "Electromagnetic wave propagation in media with indefinite permittivity and permeability tensors," *Phys. Rev. Lett.* **90**(7), 077405077409 (2003).
 32. I. V. Lindell, S. A. Tretyakov, K. I. Nikoskinen, and S. Ilvonen, "BW media media with negative parameters, capable of supporting backward waves," *Microw. Opt. Technol. Lett* **31**, 129 (2001).
 33. J. Yang, X. Hu, X. Li, Z. Liu, X. Jiang, and J. Zi, "Cancellation of reflection and transmission at metamaterial surfaces," *Opt. Lett.* **35**, 16 (2010).
 34. H. Hu, D. Ji, X. Zeng, K. Liu, and Q. Gan, "Rainbow Trapping in Hyperbolic Metamaterial Waveguide," *Sci. Rep.* **3**, 1249 (2013).
 35. W. T. Lu and S. Sridhar, "Slow light, open-cavity formation, and large longitudinal electric field on a slab waveguide made of indefinite permittivity metamaterials," *Phys. Rev. A* **82**, 013811 (2010).
 36. C. Rizza, A. Ciattoni, and E. Palange, "Two-peaked and flat-top perfect bright solitons in nonlinear metamaterials with epsilon near zero," *Phys. Rev. A* **83**, 053805 (2011).
 37. M. A. Vincenti, D. de Ceglia, A. Ciattoni, and M. Scalora, "Singularity-driven second- and third-harmonic generation at ϵ -near-zero crossing points," *Phys. Rev. A* **84**, 063826 (2011).
 38. A. Ciattoni, C. Rizza, E. Palange, "Transverse power flow reversing of guided waves in extreme nonlinear metamaterials," *Opt. Lett.* **35**, 11911 (2010).
 39. A. Ciattoni, C. Rizza, and E. Palange, "Transmissivity directional hysteresis of a nonlinear metamaterial slab with very small linear permittivity," *Opt. Lett.* **35**, 2130 (2010).
 40. R. J. Pollard, A. Murphy, W. R. Hendren, P. R. Evans, R. Atkinson, G. A. Wurtz, A.V. Zayats, and V.A. Podolskiy, "Optical Nonlocalities and Additional Waves in Epsilon-Near-Zero Metamaterials," *Phys. Rev. Lett.* **102**, 127405 (2009).
 41. A. A. Orlov, P. M. Voroshilov, P. A. Belov, and Y. S. Kivshar, "Engineered optical nonlocality in nanostructured metamaterials," *Phys. Rev. B* **84**, 045424 (2011).
 42. D. J. Bergman, "The dielectric constant of a composite material - a problem in classical physics," *Phys. Rep.* **43**, 377-407 (1978).
-

1. Introduction

With recent advances in nanoscale fabrication of metal-dielectric multilayers and arrays of rods, hybrid structures can now be created that absorb a substantial portion of incident electromagnetic (EM) radiation. In conventional approaches, strong absorption was achieved by utilizing materials that had either high loss or large thickness. Nowadays, with the advent of metamaterials, absorbing structures can be created that harness plasmonic excitations or implement high impedance components [1] that have extreme values [2–5] of the permittivity ϵ or permeability μ . In close connection with these developments, there has also been a substantial amount of research lately involving anisotropic metamaterials, where now ϵ and μ are tensors that have in general differing components along the three coordinate axes. An important type of anisotropic metamaterial is one whose corresponding orthogonal tensor components are of opposite sign, sometimes referred to as indefinite media [6]. When such structures are described by a diagonal tensor, the corresponding dispersion relation permits wavevectors that lie within a hyperbolic isofrequency surface, and hence such a material is also called a hyperbolic metamaterial (HMM). The inclusion of HMM elements in many designs can be beneficial due to their inherent nonresonant character, thus limiting loss effects [7].

The earliest HMM construct involving bilayers of anisotropic media was discussed in the context of bandpass spatial filters with tunable cutoffs [6]. For wavelengths λ in the visible spectrum, an effective HMM was modeled using arrays of metallic nanowires [8] spaced apart distances much smaller than λ , thus avoiding the usual problems associated with resonances. Periodic arrays of carbon nanotubes [9] have been shown to exhibit HMM characteristics in the THz spectral range. Other possibilities involve metal-dielectric layers: The inclusion of active media in metal-dielectric multilayers can result in improved HMM-based imaging devices [10]. For certain layer configurations, nonlocal effects [11], which depending on geometry [12], can limit the number of accessible photonic states [13]. The absorption in thin films has been shown experimentally to be enhanced when in contact with a multilayered HMM substrate [14]. Rather than using metallic components, tunable graphene can switch between a hyperbolic and conventional material via a gate voltage [15]. The HMM dispersion can be tuned in gyromagnetic/dielectric [16] and semiconductor/dielectric structures [17]. Slabs of semiconductors can also exhibit tunability by photogenerating a grating via variations in the carrier density caused by two incident beams, revealing a hyperbolic character [18].

Increased absorption can also be achieved by incorporating a grating with the HMM, so that by introducing surface corrugations, or grooves, light can diffract and generate a broad spectrum of wave vectors into the HMM layer. These wavevectors can couple via surface modes [19] due to the impedance mismatch at the various openings. Grating lines were patterned above a layered Au/TiO₂ HMM structure, creating a “hypergrating” capable of exciting both surface and bulk plasmons [20]. By judiciously designing the materials below the grating, it can be possible to absorb a considerable fraction of the diffracted EM field. Indeed, a HMM comprised of arrays of silver nanowires was experimentally shown to reduce the reflectance by introducing surface corrugations [21]. Spherical nanoparticles deposited on planar HMM structures also resulted in reduced reflectance due to the increased density of photonic states [22].

In this paper we show that near-perfect absorption of EM radiation can arise in a simple HMM structure adjacent to a metal. We investigate a range of frequencies where the permittivity components perpendicular and parallel to the interfaces are of opposite sign. We consider two possibilities: when the HMM dispersion relation is of type-1 or type-2, which for our geometry corresponds to $\epsilon_x > 0$, $\epsilon_z < 0$ or $\epsilon_x < 0$, $\epsilon_z > 0$ respectively (see Fig. 1). We show that for those λ leading to the real part of the permittivity component perpendicular to the interfaces (ϵ_z) nearly vanishing, an intricate balance between material loss and structure thickness (τ) yields a broad range of incident angles θ and τ in which nearly the entire EM wave is absorbed. These

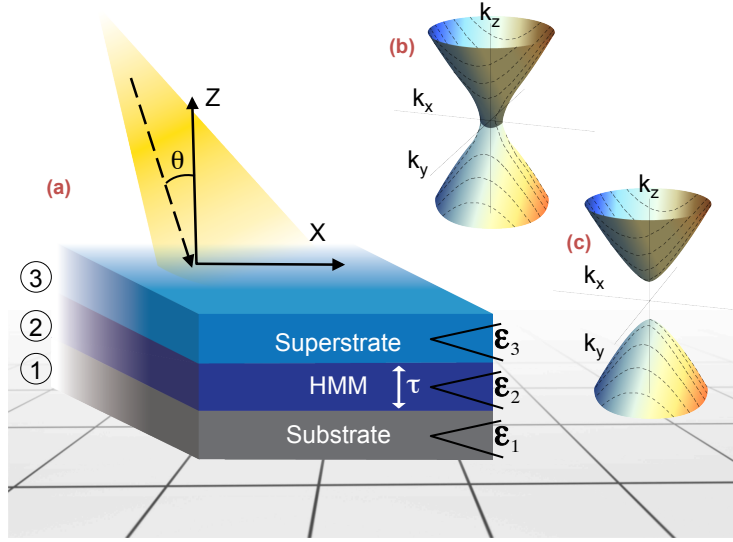


Fig. 1. (a) Schematic of the hyperbolic metamaterial configuration: The HMM layer of thickness τ is bordered by a semi-infinite superstrate and substrate. The permittivities ϵ_i ($i=1,2,3$) are in general anisotropic. The incident field is polarized in the $x-z$ plane at an angle θ . (b) Dispersion contours for a type-2 HMM where $\epsilon_x < 0$, and $\epsilon_z > 0$ and (c) for a type-1 HMM with $\epsilon_x > 0$, and $\epsilon_z < 0$.

findings are absent in conventional anisotropic “elliptical” structures.

2. Methods

We assume that the incident EM wave propagates with wave vector in the $x-z$ plane with polarization (E_x, E_z, B_y) (p -polarized) or (E_y, B_x, B_z) (s -polarized). Once the wave enters the anisotropic medium, its polarization state can then split into linear combinations of both TE and TM polarizations [23]. Consider an unbounded diagonally anisotropic medium described by homogeneous parameters $(\epsilon_x, \epsilon_y, \epsilon_z)$ and (μ_x, μ_y, μ_z) , where it is always possible to choose principal coordinate axes so that the permittivity and permeability are diagonal. Assuming a harmonic time dependence, $\exp(-i\omega t)$, for the EM fields, Maxwell’s equations give the corresponding wave equations for the electric field components E_x and E_y :

$$\frac{\partial^2 E_x}{\partial z^2} + \left[\left(\frac{\omega}{c} \right)^2 \epsilon_x \mu_y - \left(\frac{\epsilon_x}{\epsilon_z} \right) k_x^2 \right] E_x = 0, \quad (1)$$

$$\frac{\partial^2 E_y}{\partial z^2} + \left[\left(\frac{\omega}{c} \right)^2 \epsilon_y \mu_x - \left(\frac{\mu_x}{\mu_z} \right) k_x^2 \right] E_y = 0. \quad (2)$$

Equations (1) and (2) illustrate that the wave equations are different for E_x and E_y , resulting in two different wave vectors. In this work, we focus exclusively on p -polarization from which the nature of the HMM dispersion can be qualitatively understood. From Eq. (1), $\hat{k}_z^2 = \epsilon_x \mu_y - (\epsilon_x/\epsilon_z) \hat{k}_x^2$ (the caret symbol signifies normalization by ω/c). For this discussion we assume real valued material parameters and positive μ_y . Focusing on $\epsilon_x > 0$, we consider two scenarios (a) $\epsilon_z > 0$ and (b) $\epsilon_z < 0$, yielding the respective dispersion relations $\hat{k}_z^2/(\epsilon_x \mu_y) + \hat{k}_x^2/(\epsilon_z \mu_y) = 1$ and $\hat{k}_z^2/(\epsilon_x \mu_y) - \hat{k}_x^2/(|\epsilon_z| \mu_y) = 1$. Thus the isofrequency contours are (a) ellipses and (b) hyperbola (see e.g., Fig. 1(c) when $k_y = 0$). Moreover, for the ellipsoidal case, as \hat{k}_x increases there will be

a frequency cutoff since \hat{k}_z^2 eventually becomes negative. On the other hand, for the hyperbolic case, when \hat{k}_x increases, there is no cutoff since \hat{k}_z^2 remains positive. If $\varepsilon_x < 0$ and $\varepsilon_z > 0$, we then have the possibility of a connected hyperbola (see Fig. 2(b)).

To determine the absorbed EM energy, it is convenient to first determine the Fresnel reflection coefficient, r . The corresponding reflectance R is then given by $R = |r|^2$. For a p -polarized plane wave incident at an angle θ relative to the normal of a planar layer of thickness τ , we find,

$$r = \beta \left[\frac{(\hat{k}_{z1}\varepsilon_{x2} - \hat{k}_{z2}\varepsilon_{x1})(\hat{k}_{z2}\varepsilon_{x3} + \hat{k}_{z3}\varepsilon_{x2})e^{i\phi_2} + (\hat{k}_{z1}\varepsilon_{x2} + \hat{k}_{z2}\varepsilon_{x1})(\hat{k}_{z2}\varepsilon_{x3} - \hat{k}_{z3}\varepsilon_{x2})e^{-i\phi_2}}{(\hat{k}_{z1}\varepsilon_{x2} - \hat{k}_{z2}\varepsilon_{x1})(\hat{k}_{z2}\varepsilon_{x3} - \hat{k}_{z3}\varepsilon_{x2})e^{i\phi_2} + (\hat{k}_{z1}\varepsilon_{x2} + \hat{k}_{z2}\varepsilon_{x1})(\hat{k}_{z2}\varepsilon_{x3} + \hat{k}_{z3}\varepsilon_{x2})e^{-i\phi_2}} \right], \quad (3)$$

where the semi-infinite substrate and superstrate are in general anisotropic (see Fig. 1). The details can be found in Sec. 4. We define,

$$\beta = \exp(-2i\phi_3), \quad (4)$$

where

$$\phi_j \equiv (\omega/c)\hat{k}_{zj}\tau, \quad (5)$$

and

$$\hat{k}_{zj}^2 \equiv \varepsilon_{xj}\mu_{yj} - (\varepsilon_{xj}/\varepsilon_{zj})\hat{k}_x^2. \quad (6)$$

The index j labels the regions 1, 2 or 3 (see Fig. 1). In all cases below, the incident beam is in vacuum (region 3) so that $\hat{k}_x = \sin\theta$, which is conserved across the interface. The frequency dispersion in the HMM takes the Drude-like form: $\varepsilon_{z2} = a + ib$, where $a = 1 - \alpha^2/[1 + (\alpha f)^2]$, and $b = \alpha^3 f/[1 + (\alpha f)^2]$. Here, $\alpha \equiv \lambda/\lambda_c$, $f = 0.02$, and the characteristic wavelength, $\lambda_c = 1.6\mu\text{m}$. When discussing the two types of HMM, the permittivity parallel to the interface is described using $\varepsilon_{x2} = \pm 4 + 0.1i$ for type-1 (+) and type-2 (-). The wavelength range considered here, where the system exhibits HMM behavior is consistent with experimental work involving HMM semiconductor hybrids [24].

When the surrounding media is air and the central layer is a diagonally anisotropic HMM, setting the numerator of (3) to zero leads to a set of conditions on the wavevector components that results in a complete absence of reflection ($R = 0$):

$$\hat{k}_x^2 = \varepsilon_{z2} \left(\frac{\varepsilon_{x2} - \mu_{y2}}{\varepsilon_{z2}\varepsilon_{x2} - 1} \right); \quad \hat{k}_{z2}^2 = \varepsilon_{x2}^2 \left(\frac{\varepsilon_{z2}\mu_{y2} - 1}{\varepsilon_{z2}\varepsilon_{x2} - 1} \right) \quad (7)$$

$$\hat{k}_x^2 = \varepsilon_{z2}\mu_{y2} - \left(\frac{\varepsilon_{z2}}{\varepsilon_{x2}} \right) \left(\frac{n\lambda}{2\tau} \right)^2; \quad \hat{k}_{z2}^2 = \left(\frac{n\lambda}{2\tau} \right)^2, \quad (8)$$

where n is an integer. The \hat{k}_x in Eq. (7) corresponds to the classic Brewster angle condition for isotropic media: $\hat{k}_z^2\varepsilon_{x2}^2 = \hat{k}_{z2}^2$, and the \hat{k}_x in Eq. (8) corresponds to a standing wave condition in the z -direction. In either case, when Eqs. (7) or (8) is satisfied, a minimum in R arises. Under the Brewster angle condition in Eq. (7), a simple rearrangement shows that $\hat{k}_x^2(\varepsilon_{x2} - \varepsilon_{z2}^{-1}) = \varepsilon_{x2} - \mu_{y2}$. This implies that if we choose $\varepsilon_{x2} = \mu_{y2}$ and $\varepsilon_{x2}\varepsilon_{z2} = 1$, then we should have $R = 0$ for any value of $\hat{k}_x = \sin\theta$. This choice of anisotropic material parameters is similar to the perfectly matched layer (PML) approach to eliminating unwanted reflection from absorbing computational domain boundaries, especially in time-domain [25,26] and frequency-domain algorithms [27,28]. Note that such a PML medium is somewhat artificial since $\varepsilon_{x2} = \varepsilon_{z2}^{-1}$ implies sources in region 2. Nonetheless such a concept is successful for absorbing layers designed to simulate an infinite computational domain.

We now illustrate the important case of a HMM backed by a perfectly conducting metal, and the near-perfect absorption that can arise. As is appropriate for HMM structures, we also

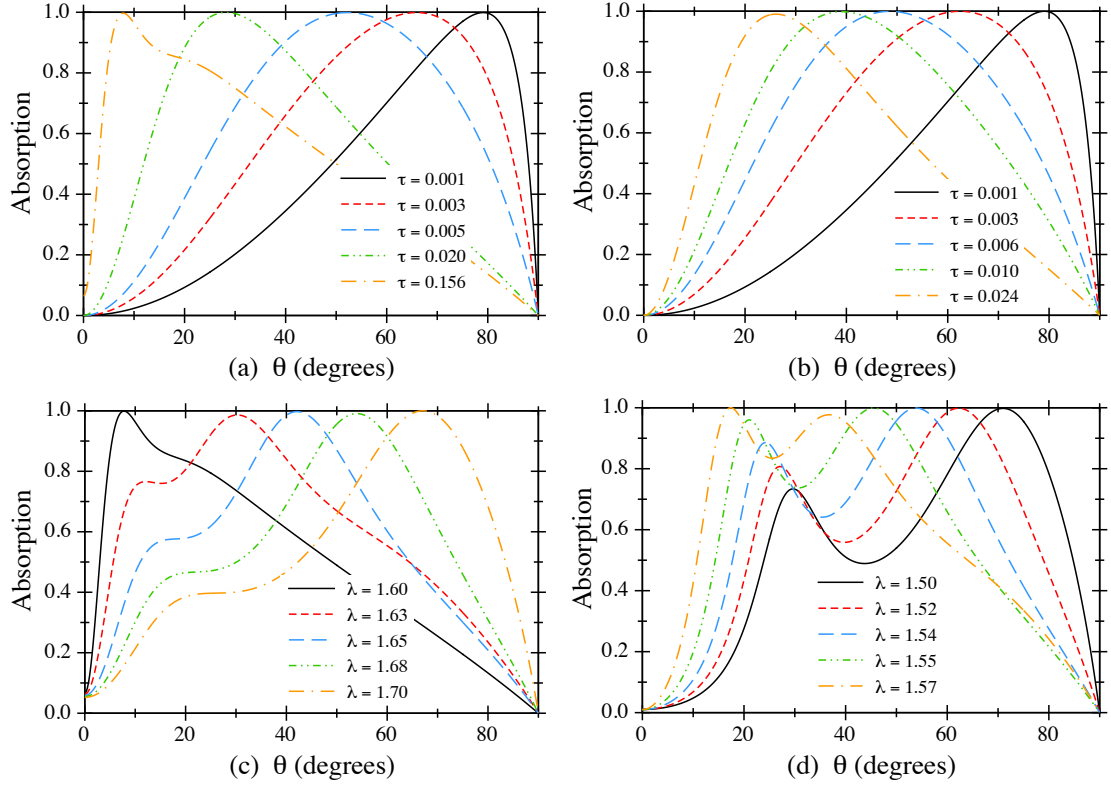


Fig. 2. Absorption as a function of incident angle θ . The superstrate is air, and the HMM layer is supported by a perfectly conducting substrate. In (a) and (b) a range of HMM widths τ are studied (legend units are in microns). In (a) $\Re(\epsilon_{2x}) > 0$ and $\Re(\epsilon_{2z}) < 0$ (type-1 HMM), and in (b) $\Re(\epsilon_{2x}) < 0$, and $\Re(\epsilon_{2z}) > 0$ (type-2 HMM). For both panels (a) and (b), $\lambda \approx \lambda_c$ so that $\Re(\epsilon_{2z}) \approx 0$. Panels (c) and (d) show the effects of varying λ for both the type-1 and type-2 cases respectively. For those cases τ is fixed at $0.16 \mu\text{m}$. For normal incidence ($\theta = 0^\circ$), there is generally little absorption (high reflectance). Remarkably, for a range of HMM widths and wavelengths there are strong absorption peaks spanning a broad range of θ .

consider the regime where all materials are nonmagnetic ($\boldsymbol{\mu} = 1$). The reflection coefficient in Eq. (3) then becomes,

$$r = e^{-2i\phi} \left[\frac{(\hat{k}_{z2} + \hat{k}_z \varepsilon_{x2})e^{i\phi_2} - (\hat{k}_{z2} - \hat{k}_z \varepsilon_{x2})e^{-i\phi_2}}{(\hat{k}_{z2} - \hat{k}_z \varepsilon_{x2})e^{i\phi_2} - (\hat{k}_{z2} + \hat{k}_z \varepsilon_{x2})e^{-i\phi_2}} \right], \quad (9)$$

where $\phi \equiv (\omega/c)\hat{k}_z\tau$, and $\hat{k}_z = \cos\theta$. It is readily verified that for lossless media, Eq. (9) yields perfect reflection ($|r|^2=1$) as expected. In the absence of transmission, the absorption, A , is simply written as $A = 1 - R$.

3. Results

Figure 2 shows the absorption as a function of incident angle θ for both types of HMM: type-1, $\Re\{\varepsilon_{2x}\} > 0$, $\Re\{\varepsilon_{2z}\} < 0$ (panels a and c), and type-2, $\Re\{\varepsilon_{2x}\} < 0$, $\Re\{\varepsilon_{2z}\} > 0$ (panels b and d). Since $\lambda \approx \lambda_z$, we have also the condition, $\Re(\varepsilon_{2z}) \approx 0$. There cannot be any substrate transmission and thus $R < 1$ is due to intrinsic HMM losses. In terms of practical designs, it is important to determine the range of sub-wavelength HMM layer thicknesses that can admit perfect absorption. Thus Figs. 2(a) and (b) explore differing τ ranging from 0.001 to 0.156 μm . Although the relative sign of ε_{x2} and ε_{z2} usually plays a pivotal role, for extremely thin HMM widths this is not the case. Indeed in the regime of small ϕ_2 , Eq. (9) simplifies to,

$$r = \frac{\hat{k}_z + i2\pi\hat{\tau}(1 - \hat{k}_x^2/\varepsilon_{z2})}{-\hat{k}_z + i2\pi\hat{\tau}(1 - \hat{k}_x^2/\varepsilon_{z2})}, \quad (10)$$

which is independent of ε_{x2} . Here we have introduced the dimensionless thickness: $\hat{\tau} \equiv \omega\tau/c$. Setting the numerator of r to zero gives the angle, θ_c , where the reflectance vanishes:

$$\theta_c = \cos^{-1} \left[(i\varepsilon_{z2} + \sqrt{(2\hat{\tau})^2(1 - \varepsilon_{z2}) - \varepsilon_{z2}^2}) / (2\hat{\tau}) \right]. \quad (11)$$

In Fig. 2(a), for the incident wavelength of 1.601 μm , the approximate absorption angles are found from taking the real part of Eq. (11), giving, $\theta_c \approx 79^\circ, 66^\circ, 52^\circ, 28^\circ$, and 11° , in order of increasing τ . Deviations in the angle predicted from Eq. (11) arise for larger τ as higher order corrections are needed. As the thickness τ decreases, near-perfect absorption shifts towards grazing incidences, in agreement with Eq. (11) where as $\tau \rightarrow 0$, $\theta_c \rightarrow \pi/2$. For the type-2 HMM, similar trends are seen in Fig. 2(b), where $\lambda = 1.59\mu\text{m}$ and the near-perfect absorption angles were found to agree well with Eq. (11). It is apparent that for a type-2 HMM, the angular range of near-perfect absorption exhibits a greater sensitivity to τ than the type-1 case shown. In both cases (a) and (b), near-perfect absorption can be controlled over nearly the whole angular range by properly choosing the effective material thicknesses. When calculating the regions of high absorption, $\Im(\varepsilon_{z2})$ plays a significant role when $\Re(\varepsilon_{z2}) \approx 0$. This is consistent with anisotropic leaky-wave structures [4] and coherent perfect absorbers [5]. Although more difficult to achieve in practice, subwavelength isotropic slabs where the permittivity and permeability simultaneously vanish, can exhibit perfect absorption for small loss and a perfectly conducting metal backing [29]. Additional control of absorption may also be possible with the introduction of gain media [10].

Next we investigate how varying the wavelength of the source beam affects the absorption features. In Figs. 2(c) and (d) the thickness τ is set to 0.16 μm for both the type-1 and type-2 HMM cases respectively. For the type-1 HMM (panel c), as λ increases beyond λ_z , the wavelength-dependent ε_{z2} shifts so that its real part becomes more negative. The corresponding absorption peaks then migrate towards $\theta = 90^\circ$. The opposite trend occurs for the type-2

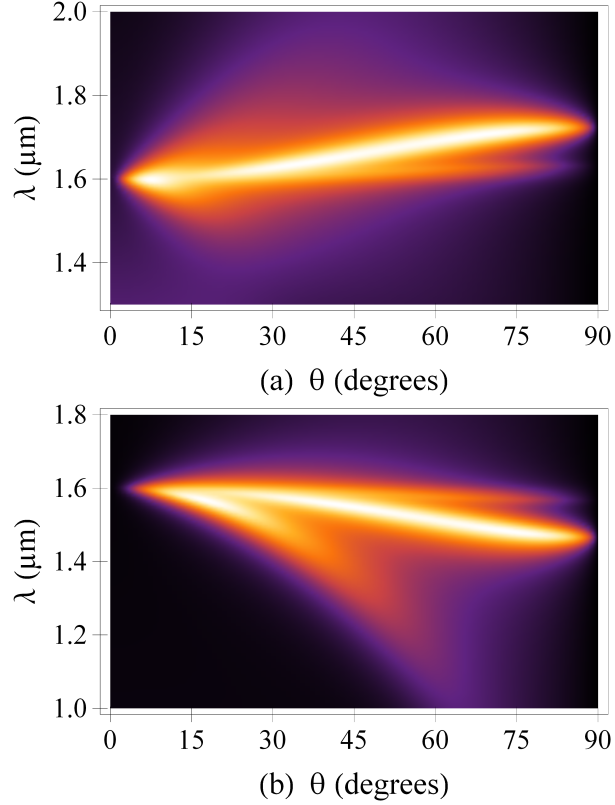


Fig. 3. Density plots showing absorption as a function of incident wavelength λ and angle θ . Bright regions correspond to high absorption. The HMM thickness in both plots is $\tau = 0.16\mu\text{m}$. The characteristic wavelength, $\lambda_z = 1.6\mu\text{m}$ separates the HMM regions according to (a) type-1: $\epsilon_{x2} > 0$ and $\epsilon_{z2} < 0$ for $\lambda > 1.6\mu\text{m}$, and (b) type 2: $\epsilon_{x2} < 0$, and $\epsilon_{z2} > 0$ for $\lambda < 1.6\mu\text{m}$. Thus we find that when the metamaterial is effectively hyperbolic, absorption can be strongly enhanced.

case, where increasing λ from $\lambda = 1.5\mu\text{m}$ causes $\Re(\epsilon_{z2})$ (which is positive at this wavelength) to approach zero. Consequently, the observed double-peaked absorption shifts towards normal incidence, consistent with the trends above and Eq. (11), where as $\lambda \rightarrow \lambda_z$ (and hence $\Re(\epsilon_{z2}) \rightarrow 0$), the angle of near-perfect absorption tends to zero. It is worth noting that if the HMM is replaced by an isotropic metallic layer like silver, the condition where the permittivity is near zero is consistent with the generation of bulk longitudinal collective oscillations of the free electrons. This type of excitation can produce moderate (but less than 100%) absorption when there is minimal intrinsic material loss.

For the case of vacuum superstrate and substrate, Eq. (3) reveals that when $\sin \phi_2 = 0$, then $R = 0$. If on the other hand, both substrate and superstrate are perfectly conducting, then setting the denominator of (3) equal to zero also yields $\sin \phi_2 = 0$, which coincides with the dispersion relation for guided waves in an HMM layer. Equation (8) shows that when $n = 0$, $\hat{k}_x^2 = \epsilon_{z2}\mu_{y2}$ and $\hat{k}_z^2 = 0$, corresponding to a TEM mode which is essentially a plane wave confined to propagate in the x -direction. Thus if $\phi_2 = \hat{k}_{z2}\hat{t} = n\pi$, this assertion is valid if $\phi_2 \ll n\pi$. If however $\epsilon_{z2}/\epsilon_{x2} < 0$, Eq. (8) reveals that there is no guided mode cutoff for \hat{k}_x^2 .

To present a global view of the parameter space in which our anisotropic structure can

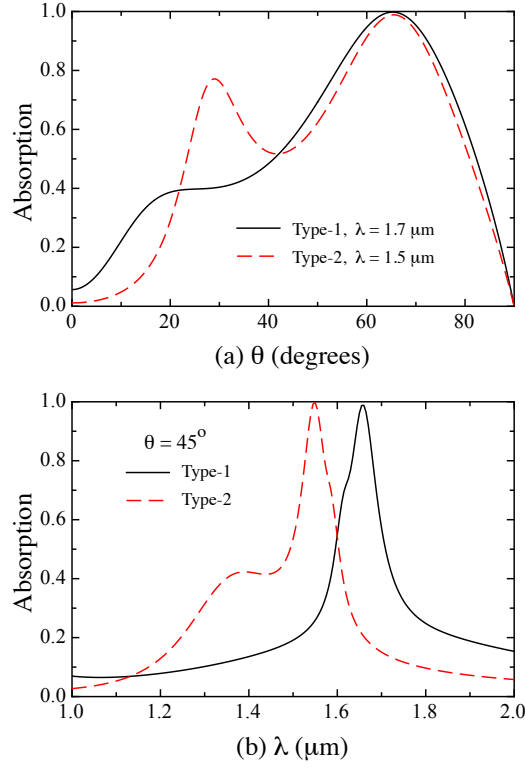


Fig. 4. Absorption as a function of incident angle θ (a) and wavelength λ (b) extracted from the high absorption regions of the density plots in Fig. 3(a) and (b).

absorb unusually large portions of incident energy, we present in Figs. 3(a) and (b), 2-D density plots that map the absorption versus λ and θ . The HMM thickness is fixed at $\tau = 0.16\mu\text{m}$, as in Figs. 2(c) and (d). In Fig. 3(a) $\epsilon_{x2} = (4, 0.1)$, so that the HMM region where $\Re(\epsilon_{z2}) < 0$ corresponds to $\lambda > \lambda_z$ (recall that $\lambda_z = 1.6\mu\text{m}$). Similarly for (b), $\epsilon_{x2} = (-4, 0.1)$, and thus the HMM region there corresponds to $\lambda < 1.6\mu\text{m}$. Figs. 4(a) and (b) are slices from Figs. 3(a) and (b). In Fig. 4(a) near-perfect absorption occurs at $\theta = 65^\circ$ for both HMM types. For $\lambda = 1.7\mu\text{m}$, $\Re(\epsilon_{x2}) = 4$ and $\Re(\epsilon_{z2}) = -0.128$ corresponding to a Type-1 HMM. For $\lambda = 1.5\mu\text{m}$, $\Re(\epsilon_{x2}) = -4$ and $\Re(\epsilon_{z2}) = 0.121$, corresponding to a Type-2 HMM. In Fig. 4(b), the Type-1 absorption peak occurs at $\lambda = 1.66\mu\text{m}$, where $\Re(\epsilon_{z2}) = -0.076$, and the Type-2 case peaks at $\lambda = 1.55\mu\text{m}$, where $\Re(\epsilon_{z2}) = 0.062$.

Further insight into this anomalous absorption can be gained from studying the balance of energy [30]. For our structure and material parameters, it suffices to compute,

$$\frac{4\pi}{c} \int_V dv \mathbf{E} \cdot \mathbf{J}^* = - \int_V dv \nabla \cdot (\mathbf{E} \times \mathbf{H}^*) - \frac{i\omega}{c} \int_V dv [\epsilon_{x2}^* |E_{x2}|^2 + \epsilon_{z2}^* |E_{z2}|^2 - |H_{y2}|^2]. \quad (12)$$

Since we have incorporated the conductive part of the HMM into the dielectric response, the \mathbf{J} term is absent. In all of the near-perfect absorption examples investigated here, evaluation of Eq. (12) confirmed that the net energy flow into the HMM volume, V , is converted into heat.

To explore further the behavior of the energy flow, we present in Fig. 5 the average power P in the HMM as a function of θ for the two cases in Fig. 4(a). Thus, panel (a) is for $\lambda = 1.7\mu\text{m}$ (type-1 HMM), and panel (b) corresponds to $\lambda = 1.5\mu\text{m}$ (type-2 HMM). The average power

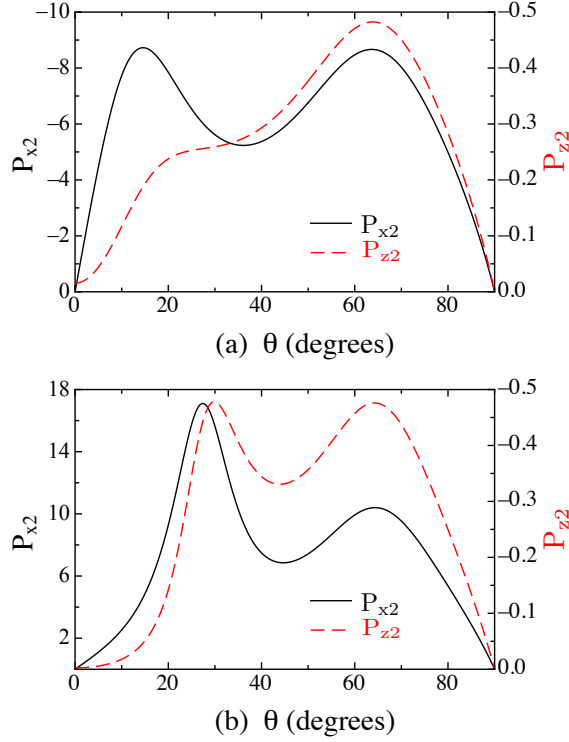


Fig. 5. The power \mathbf{P} in the HMM, normalized by the incident power in the z -direction, and plotted as a function of θ . In (a) $\lambda = 1.7 \mu\text{m}$ (type-1 HMM) and in (b) $\lambda = 1.5 \mu\text{m}$ (type-2 HMM). The material parameters are the same as in Fig. 4(c). Panel (a) reveals that energy flow parallel to the interface (P_{x2}) in the type-1 HMM is negative, which is opposite that of the vacuum region containing the incident beam.

along the x and z directions, P_{x2} and P_{z2} , is found from averaging the corresponding components of the Poynting vector over the HMM region (see Eqs. (29)). It is evident that the direction of energy flow depends on the sign of ϵ_{z2} (or equivalently whether λ is above or below λ_z). The component of \mathbf{P} normal to the interfaces (P_{z2}) must always have the same sign on both sides of the interface [31]. Its direction parallel to the interface (P_{x2}) however can be negative if the HMM is of type-1, as seen in Fig. 5(a), and is clearly opposite in direction to k_x , which is always positive. This manifestation of “negative refraction” was discussed in the context of uniaxially anisotropic media [32], certain nanowire structures [8], and observed in ZnO-based multilayers [24]. Comparing the peaks in panels (a) and (b) with Fig. 4(a), we see the correlation with the angles where near-perfect absorption occurs and those where $|P_{z2}|$ is maximal.

4. Conclusion

In conclusion, we have investigated the absorption properties of both type-1 and type-2 hyperbolic metamaterials. We found that HMMs can absorb significantly higher amounts of electromagnetic energy compared to their conventional counterparts, where $\Re(\epsilon_{x2})$ and $\Re(\epsilon_{z2})$ are both of the same sign. Our results show that the incident beam can couple to the HMM structure without recourse for a second compensating layer. We also revealed that the condition $\Re(\epsilon_z) \approx 0$ leads to near-perfect absorption over a range of frequencies, angles of incidence, and

subwavelength structure thicknesses, making the proposed structures experimentally achievable. Alternate methods exist to achieve perfect absorption, including periodic layers of silver and conventional dielectrics that depending on the direction of incident wave propagation and loss, can exhibit anisotropic behavior that cancels the reflected and transmitted waves simultaneously [33]. Our HMM with metallic backing is a different configuration in which no energy can be transmitted, and the inherently finite width of the structure means that there are no Bloch wave excitations. Arrays of metal-dielectric films can serve as an effective HMM waveguide taper, resulting in light localization and enhanced absorption [34], however, the modes responsible for “slow-light” are very sensitive to the presence of loss [35].

When the incident wavelength results in the dielectric response of the metamaterial possessing a nearly vanishing component of the permittivity, contributions from nonlinear effects and/or spatial dispersions can become important. Nonlinear effects can in this case generate interesting phenomena such as two-peaked or flat solitons [36], as well as additional venues for second- and third-harmonic generation [37], and guided waves whose Poynting vector undergoes localized reversal [38]. Since the nonlinear part of the dielectric response can now be of the same order as the (small) linear part, the transmissivity can exhibit directional hysteresis behavior [39]. Spatial dispersion can moreover lead to the appearance of additional EM waves, as was reported for nanorods [40]. For metal-dielectric structures, nonlocality arising from the excitation of surface plasmons can also lead to significant corrections [41] to conventional effective medium theories [42].

Appendix: Poynting’s Theorem

In this section we present the details on how the EM fields are straightforwardly calculated for determining the reflectance and energy flow in HMM structures. We have considered in this paper diagonally anisotropic HMM layers ($\epsilon_x, \epsilon_z, \mu_y$). We also assume that EM wave propagation and polarization is in the x - z plane. The wave equation for E_x is thus,

$$\frac{\partial^2 E_x}{\partial z^2} + \left[\left(\frac{\omega}{c} \right)^2 \epsilon_x \mu_y - \left(\frac{\epsilon_x}{\epsilon_z} \right) k_x^2 \right] E_x = 0. \quad (13)$$

Taking into account that $\nabla \cdot \mathbf{D} = \nabla \cdot \mathbf{B} = 0$, this yields the electric field solutions in their respective media as,

$$\mathbf{E}_1 = \left[A \left\{ \hat{x} + \hat{z} \left(\frac{\hat{k}_x \epsilon_{x1}}{\hat{k}_{z1} \epsilon_{z1}} \right) \right\} e^{-ik_{z1}z} \right] e^{ik_x x}, \quad (14)$$

$$\mathbf{E}_2 = \left[G \left\{ \hat{x} - \hat{z} \left(\frac{\hat{k}_x \epsilon_{x2}}{\hat{k}_{z2} \epsilon_{z2}} \right) \right\} e^{ik_{z2}z} + F \left\{ \hat{x} + \hat{z} \left(\frac{\hat{k}_x \epsilon_{x2}}{\hat{k}_{z2} \epsilon_{z2}} \right) \right\} e^{-ik_{z2}z} \right] e^{ik_x x}, \quad (15)$$

$$\mathbf{E}_3 = \left[C \left\{ \hat{x} - \hat{z} \left(\frac{\hat{k}_x \epsilon_{x3}}{\hat{k}_{z3} \epsilon_{z3}} \right) \right\} e^{ik_{z3}z} + I \left\{ \hat{x} + \hat{z} \left(\frac{\hat{k}_x \epsilon_{x3}}{\hat{k}_{z3} \epsilon_{z3}} \right) \right\} e^{-ik_{z3}z} \right] e^{ik_x x}. \quad (16)$$

Similarly, the components of the magnetic field are written,

$$\mathbf{H}_1 = -\hat{y} \left(\frac{\epsilon_{x1}}{\hat{k}_{z1}} \right) A e^{-ik_{z1}z} e^{ik_x x}, \quad (17)$$

$$\mathbf{H}_2 = \hat{y} \left(\frac{\epsilon_{x2}}{\hat{k}_{z2}} \right) \left[G e^{ik_{z2}z} - F e^{-ik_{z2}z} \right] e^{ik_x x}, \quad (18)$$

$$\mathbf{H}_3 = \hat{y} \left(\frac{\epsilon_{x3}}{\hat{k}_{z3}} \right) \left[C e^{ik_{z3}z} - I e^{-ik_{z3}z} \right] e^{ik_x x}. \quad (19)$$

The I terms represent the incident field. The quantities \hat{k}_{zj} and ϕ_j are defined in Eqs. (5) and (6). Utilizing matching boundary conditions for the tangential components of the electric and magnetic fields permits calculation of the coefficients,

$$A = \frac{4e^{-i\phi_3}\hat{k}_{z1}\hat{k}_{z2}\varepsilon_{x2}\varepsilon_{x3}}{\mathcal{G}^- \mathcal{F}^- e^{i\phi_2} + \mathcal{G}^+ \mathcal{F}^+ e^{-i\phi_2}}; \quad C = \beta \left[\frac{\mathcal{G}^- \mathcal{F}^+ e^{i\phi_2} + \mathcal{G}^+ \mathcal{F}^- e^{-i\phi_2}}{\mathcal{G}^- \mathcal{F}^- e^{i\phi_2} + \mathcal{G}^+ \mathcal{F}^+ e^{-i\phi_2}} \right], \quad (20)$$

$$F = \frac{2e^{-i\phi_3}\hat{k}_{z2}\varepsilon_{x3}\mathcal{G}^+}{\mathcal{G}^- \mathcal{F}^- e^{i\phi_2} + \mathcal{G}^+ \mathcal{F}^+ e^{-i\phi_2}}; \quad G = \frac{-2e^{-i\phi_3}\hat{k}_{z2}\varepsilon_{x3}\mathcal{G}^-}{\mathcal{G}^- \mathcal{F}^- e^{i\phi_2} + \mathcal{G}^+ \mathcal{F}^+ e^{-i\phi_2}}, \quad (21)$$

where β is given in Eq. (4). We also define,

$$\mathcal{F}^\pm = \hat{k}_{z3}\varepsilon_{x2} \pm \hat{k}_{z2}\varepsilon_{x3}, \quad (22)$$

$$\mathcal{G}^\pm = \hat{k}_{z2}\varepsilon_{x1} \pm \hat{k}_{z1}\varepsilon_{x2}, \quad (23)$$

where ε_{xj} describe the media for regions $j = 1, 2, 3$, and k_{zj} is defined in Eq. (6). The caret symbol signifies that wavenumber components k_x and k_{zj} have been normalized to ω/c . In general, \hat{k}_x can be any value, but for the case of an incident plane wave in vacuum, $\hat{k}_x = \sin \theta$.

For time-harmonic fields, consider now the integral,

$$\frac{1}{2} \frac{4\pi}{c} \int_V dv \mathbf{E} \cdot \mathbf{J}^* = -\frac{1}{2} \int_V dv \nabla \cdot (\mathbf{E} \times \mathbf{H}^*) - \frac{i\omega}{2c} \int_V dv [\mathbf{E} \cdot \mathbf{D}^* - \mathbf{H}^* \cdot \mathbf{B}], \quad (24)$$

where we have used,

$$\nabla \times \mathbf{H} = \frac{4\pi}{c} \mathbf{J} - \frac{i\omega}{c} \mathbf{D} \quad ; \quad \nabla \times \mathbf{E} = \frac{i\omega}{c} \mathbf{B}. \quad (25)$$

The media are diagonally anisotropic with $\mathbf{D} = \boldsymbol{\varepsilon} \cdot \mathbf{E}$ and $\mathbf{B} = \boldsymbol{\mu} \cdot \mathbf{H}$. Inserting Eqs. (15) and (18) into Eq. (24) yields the following energy conservation relationships,

$$\begin{aligned} \frac{i\omega}{2c} \int_0^\tau dz E_{2x} D_{2x}^* &= \frac{i\varepsilon_{2x}^*}{2} \left[|G|^2 \left(\frac{e^{-2\tau\Im(k_{2z})} - 1}{-2\Im(\hat{k}_{2z})} \right) + |F|^2 \left(\frac{e^{2\tau\Im(k_{2z})} - 1}{2\Im(\hat{k}_{2z})} \right) \right. \\ &\quad \left. + 2\Re \left\{ GF^* \left(\frac{e^{2i\tau\Re(k_{2z})} - 1}{2i\Re(\hat{k}_{2z})} \right) \right\} \right], \end{aligned} \quad (26)$$

$$\begin{aligned} \frac{i\omega}{2c} \int_0^\tau dz E_{2z} D_{2z}^* &= \frac{i\varepsilon_{2z}^*}{2} \left| \frac{\hat{k}_x \varepsilon_{2x}}{\hat{k}_{2z} \varepsilon_{2z}} \right|^2 \left[|G|^2 \left(\frac{e^{-2\tau\Im(k_{2z})} - 1}{-2\Im(\hat{k}_{2z})} \right) \right. \\ &\quad \left. + |F|^2 \left(\frac{e^{2\tau\Im(k_{2z})} - 1}{2\Im(\hat{k}_{2z})} \right) - 2\Re \left\{ GF^* \left(\frac{e^{2i\tau\Re(k_{2z})} - 1}{2i\Re(\hat{k}_{2z})} \right) \right\} \right], \end{aligned} \quad (27)$$

$$\begin{aligned} \frac{i\omega}{2c} \int_0^\tau dz H_{2y} B_{2y} &= \frac{i\mu_{2y}}{2} \left| \frac{\varepsilon_{2x}}{\hat{k}_{2z}} \right|^2 \left[|G|^2 \left(\frac{e^{-2\tau\Im(k_{2z})} - 1}{-2\Im(\hat{k}_{2z})} \right) \right. \\ &\quad \left. + |F|^2 \left(\frac{e^{2\tau\Im(k_{2z})} - 1}{2\Im(\hat{k}_{2z})} \right) - 2\Re \left\{ GF^* \left(\frac{e^{2i\tau\Re(k_{2z})} - 1}{2i\Re(\hat{k}_{2z})} \right) \right\} \right], \end{aligned} \quad (28)$$

where the x and y integrations over V are omitted.

Finally, the time-averaged Poynting vector in V is $\mathbf{S} = \mathbf{E} \times \mathbf{H}^*/2$, giving the result,

$$S_{2x}(z) = \left(\frac{\hat{k}_x}{\varepsilon_{z2}} \right) \left| \frac{\varepsilon_{x2}}{\hat{k}_{z2}} \right|^2 \left[|G|^2 e^{-2z\Im(k_{2z})} + |F|^2 e^{2z\Im(k_{2z})} - 2\Re \left(GF^* e^{2iz\Re(k_{2z})} \right) \right], \quad (29)$$

$$S_{2z}(z) = \left(\frac{\varepsilon_{x2}}{\hat{k}_{z2}} \right)^* \left[|G|^2 e^{-2z\Im(k_{2z})} - |F|^2 e^{2z\Im(k_{2z})} - 2i\Im \left(GF^* e^{2iz\Re(k_{2z})} \right) \right]. \quad (30)$$